

A novel electrospray-based ion mobility spectrometer

Ben Bathgate, Eric C. S. Cheong, and Christopher J. Backhouse

Citation: *American Journal of Physics* **72**, 1111 (2004); doi: 10.1119/1.1645286

View online: <https://doi.org/10.1119/1.1645286>

View Table of Contents: <https://aapt.scitation.org/toc/ajp/72/8>

Published by the *American Association of Physics Teachers*

ARTICLES YOU MAY BE INTERESTED IN

Note: Design and construction of a simple and reliable printed circuit board-substrate Bradbury-Nielsen gate for ion mobility spectrometry

Review of Scientific Instruments **82**, 086103 (2011); <https://doi.org/10.1063/1.3624690>

Realization of an optical profiler: Introduction to scanning probe microscopy

American Journal of Physics **72**, 1118 (2004); <https://doi.org/10.1119/1.1648329>

Quality factors and conductances in Helmholtz resonators

American Journal of Physics **72**, 1035 (2004); <https://doi.org/10.1119/1.1677375>

Concept substitution: A teaching strategy for helping students disentangle related physics concepts

American Journal of Physics **72**, 1126 (2004); <https://doi.org/10.1119/1.1764564>

Lenz vector operations on spherical hydrogen atom eigenfunctions

American Journal of Physics **72**, 1013 (2004); <https://doi.org/10.1119/1.1758225>

A differential formulation of diffraction theory for the undergraduate optics course

American Journal of Physics **72**, 1026 (2004); <https://doi.org/10.1119/1.1758226>

AIP Author Services
English Language Editing



APPARATUS AND DEMONSTRATION NOTES

Jeffrey S. Dunham, *Editor*

Department of Physics, Middlebury College, Middlebury, Vermont 05753

This department welcomes brief communications reporting new demonstrations, laboratory equipment, techniques, or materials of interest to teachers of physics. Notes on new applications of older apparatus, measurements supplementing data supplied by manufacturers, information which, while not new, is not generally known, procurement information, and news about apparatus under development may be suitable for publication in this section. Neither the *American Journal of Physics* nor the Editors assume responsibility for the correctness of the information presented. Submit materials to Jeffrey S. Dunham, *Editor*.

A novel electrospray-based ion mobility spectrometer

Ben Bathgate, Eric C. S. Cheong, and Christopher J. Backhouse^{a)}

*Department of Electrical and Computer Engineering, University of Alberta,
Edmonton, Alberta T6G 2V4, Canada*

(Received 11 April 2003; accepted 5 December 2003)

We present a design for a low-cost ion mobility spectrometer that can be built using the equipment on hand in many electronics-oriented undergraduate laboratories. The construction of this system is based upon the use of printed circuit boards and does not require the specialized drift and sheath gases, vacuum pumps, heater assemblies, high voltage pulsers, or precision pumps that are characteristic of the systems generally reported in the literature. We demonstrate the system in the separation of ions of methanol and water in air. Despite the low cost of this system it has a performance comparable to more complex systems, with a sensitivity of approximately 100 ppm for the protein cytochrome c. This system is suitable for use as an electronics or signal-processing project, or even a biotechnology demonstration. © 2004 American Association of Physics Teachers. [DOI: 10.1119/1.1645286]

I. INTRODUCTION

Ion mobility spectrometers (IMSs) are based on the production, separation, and analysis of ions in air, in a process sometimes described as “gas phase electrophoresis.”¹ These systems have been used to analyze the composition of gas or liquid samples in applications ranging from space probes^{2,3} to drug discovery.⁴ The ability of IMS systems to operate at atmospheric pressure provides significant advantages over mass spectrometers (MSs), and, as a result, IMS systems have replaced the more complex and expensive MS systems in some applications. Ions in IMSs separate due to their relative mass, charge, and size (or cross-sectional area), whereas ions in MSs separate due to their relative mass and charge.⁵ Both methods enable the detection of drugs, explosives, biological substances (e.g., proteins and peptides), and pollutants, among other materials. IMS systems can be divided into two broad classes: those that ionize airborne compounds such as with a radioactive ionization source (e.g., ⁶³Ni), and those that produce ions from liquid samples such as electrospray (ES) sources. Compact, portable IMS systems currently available^{6,7} are based on radioactive-nickel-(⁶³Ni-) ionization,^{8–13} although various groups^{3,14} (including our own) are developing portable ES-based systems. Since ES sources are capable of ionizing nonvolatile (e.g., drugs,¹⁵ proteins¹⁶ and peptides,⁴ etc.) as well as volatile (e.g., explosives,¹⁷ etc.) materials, such systems are ideal for analyzing the liquid samples produced by the instrumentation used in the life sciences (e.g., liquid chromatographs).

Our system shown in Fig. 1 and described here has the potential for being portable, compact, and miniaturized. Although IMS systems generally use high temperatures, precision pumps, high voltage pulsers, and special drift and sheath gases, we present here a system that is based entirely upon the electronics and the electronic fabrication capabilities of a

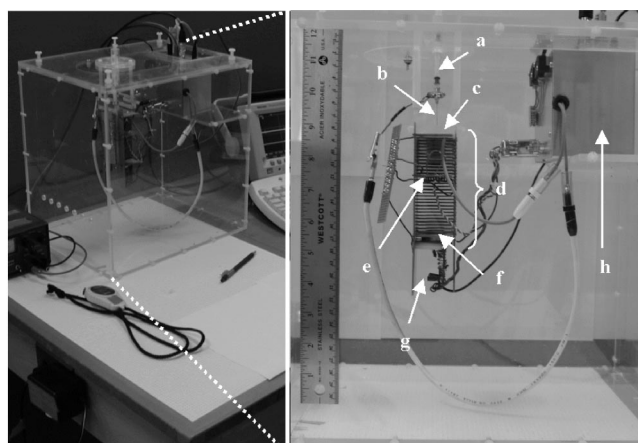


Fig. 1. Photograph of the ES-IMS system. The IMS system consists of (a) well, (b) ES needle, (c) focus grid, (d) IMS column, (e) shutter gate, (f) aperture grid and collector plate, (g) detector, and (h) control box containing the EMCO high voltage power supplies, the interlock switches, and the PIC16F877 microcontroller.

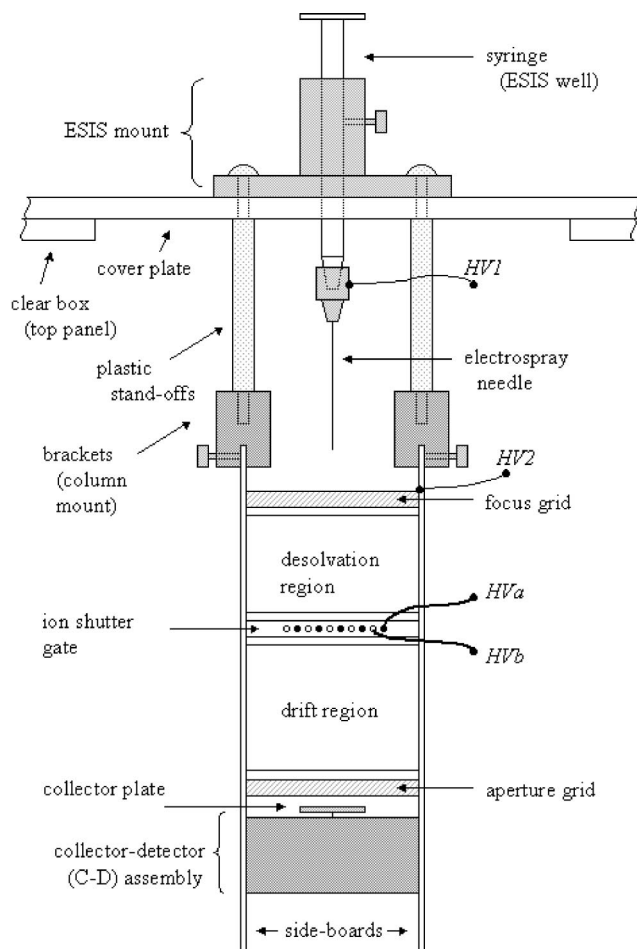


Fig. 2. Schematic diagram of the electrospray ionization source (ESIS) and the IMS drift tube/column of the printed-circuit-board (PCB)-based electrospray-ion mobility spectrometer, operated in the vertical configuration.

typical undergraduate electronics laboratory. This system is low-cost and its performance is comparable to more complex systems reported in the literature.

II. GENERAL OVERVIEW

The essence of an ES-based IMS system is to produce ions from a liquid sample and then measure their time-of-flight through the air. The arrival of the ions at the detector produces a detectable electric current. The differences in the time-of-flight of the ions produce a variation of current with time (a spectrum) and the spectrum can be used to obtain information regarding the sample composition. The system first uses the high electric field applied between a stainless steel hypodermic needle and an aperture grid to produce ions from the liquid within the needle and syringe as shown in Fig. 2. Once created, the ions are drawn through the focus (or 1st) grid into the column of the IMS system. Inside the column a uniform electric field is produced to keep the ions moving towards the detector at the end. Part of the way along the column an ion shutter gates the flow of the ions, thereby forming a pulse of ionized species that then separates into distinct pulses as the ions drift toward the detector.

As shown in Fig. 3, the electric fields draw the liquid at the needle tip into a cone-like structure referred to as a Taylor cone,^{18–20} wherein the force of attraction of the ions in

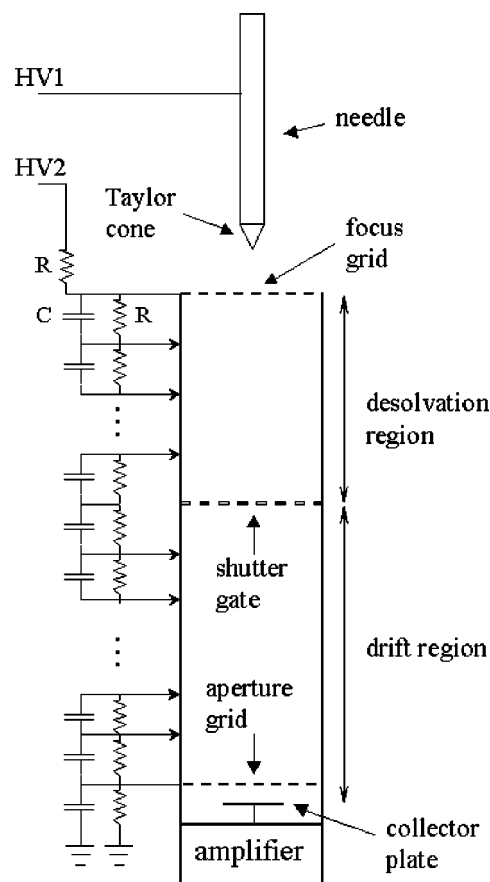


Fig. 3. Schematic diagram of the electrospray-ion mobility spectrometer, showing the resistor and capacitor arrays, the needle and the Taylor cone. Here, $R = 1\text{ M}\Omega$, $C = 100\text{ nF}$.

the liquid toward the lower potential grid balances the force of cohesion (i.e., the surface tension) of the liquid. High field effects generate ions from the tip of this Taylor cone and, although the exact mechanism of this ionization is the source of some debate, an excellent discussion is provided by Kobarle.^{21,22} The resistive divider shown in Fig. 3 serves to apply potentials to the electrode array within the column so as to produce a uniform electric field.

The remainder of the IMS system consists of two electronics circuits (an amplifier and a high-voltage switch) and an electrode array. The electrode array and the electronic circuits were built with printed circuit board (PCB) material that was patterned and cut using a PCB milling machine of the type frequently found in undergraduate laboratories. For safety the entire system was placed within a transparent Plexiglas box equipped with safety interlocks that shut off the high voltage when the box was opened.

The electrode array consists of stacked double-sided PCB segments that comprise the guard rings [used to provide uniform electric fields and screen out interference, Fig. 4(a)] and several grids [see Figs. 4(b) and 4(c)]. Each PCB segment [Figs. 4(a)–4(c)] is separated by air and held apart at the same thickness as the insulator (FR-4) layer of the board by slotting the tabs of the PCB segment into “side boards” that have evenly spaced slots [Fig. 4(d)]. This light-weight structure lends itself to producing a uniform electric field and effectively screens the ions from external interference while providing the ventilation required to allow neutral molecules to escape rather than contribute to condensation within the

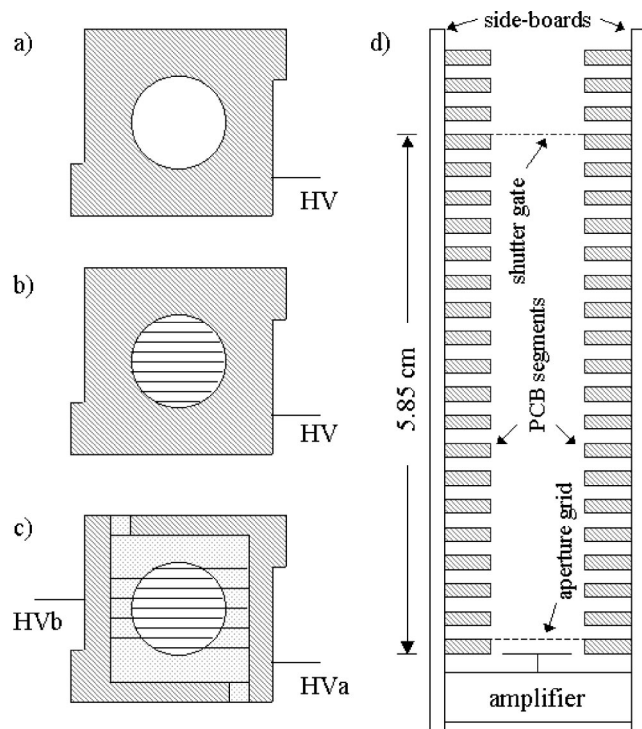


Fig. 4. Segments of the IMS column: (a) guard ring, (b) grid, (c) shutter gate, and (d) a cross-sectional view of the drift region of the IMS column. The dimensions are sides=4 cm, aperture diameter=2 cm, with a 1.1 (L) \times 0.3 cm (W) tab set on either side of elements in (a)–(c). The dot-dash line represents the shutter gate, while the dashed line represents the aperture grid; the horizontal line connected to the amplifier represents the Faraday (or collector) plate.

assembly. The focus and aperture grids are made of the segment type shown in Fig. 4(b) with grid wires 0.1 mm wide and 0.9 mm apart placed uniformly across the drift aperture.

The high voltage switch is used to control the electric fields across the grid wires within the Bradbury-Nielsen type²³ shutter gate. The ion shutter grid consists of two interdigitated sets of grid wires, each set consisting of ten wires (across the drift tube diameter) connected to one of the electrodes shown in Fig. 4(c). With high fields applied between these sets of wires, the gate [Fig. 4(c)] prevents ions

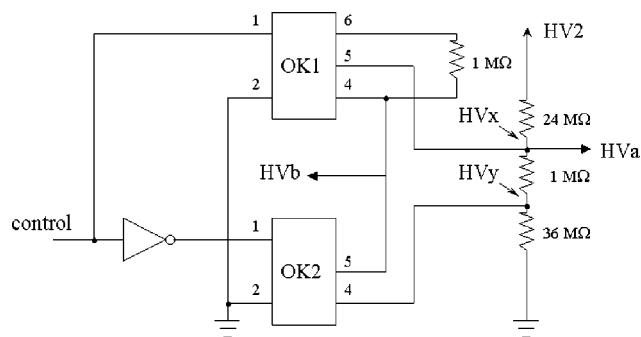


Fig. 5. Schematic diagram of the shutter gate controller circuit. OK1 and OK2 represent the high voltage phototransistor optocouplers, HV2 (at ~3 kV) the voltage supplied to the IMS column, HVa and HVb the voltage outputs to the shutter gate, and HVx (at ~1.82 kV) and HVy (at ~1.77 kV) the reference potentials for HVa and HVb. With OK1 on (and OK2 off), HVb will be held at HVx. With OK2 on, HVb will be held at HVy. HVa is always held at HVx.

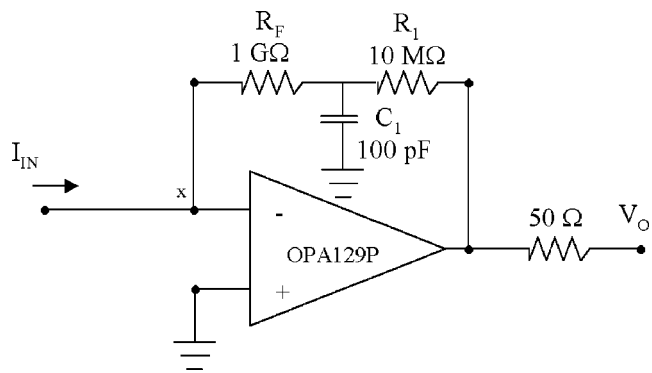


Fig. 6. Circuit schematic of the amplifier with a gain of 1.01×10^9 V/A. The input is connected to the collector plate placed at the end of the drift region of the column.

from passing into the drift region (the ions are pulled onto one or the other set of wires). When such high fields are not applied the ions pass through the shutter, and, after passing through the drift region, reach the collector plate and create a current that is detected. As shown in Fig. 5, the two sets are connected to the *a* and *b* voltage outputs of the high voltage (HV) switch circuit. When the gate is closed (voltage *a* not equal to voltage *b*) one set of grid wires is pulled down to the lower point of the voltage divider, thus setting up an orthogonal electric field between the grid wires that sweeps the ions toward the grids (annihilating them in the process).

The amplifier shown in Fig. 6 is a high impedance, low noise transconductance amplifier that produces a signal of approximately 1 millivolt for each picoampere of ion current.

To operate the system we connected these modules as shown in Fig. 7. Once the syringe had been loaded with a sample and electrospray was induced, a repetitive control signal (20 Hz) was used to open the shutter for approximately 0.3 ms each 50 ms. This same control signal was used to trigger a Tektronix TDS 3032 oscilloscope to capture the current signal versus time, thereby producing a trace referred to as a spectrum or an electropherogram. The electropherogram showed the time-of-flight of the ions produced from the sample, often allowing the identification of the constituents of the sample particularly when preceded by another separation method such as liquid chromatography.

III. CONSTRUCTION AND DESIGN

Although the details given here are specific to the equipment and approach we used, we believe that the details are sufficient to suggest alternate approaches if needed. The PCB design work was done with the professional version of the Eagle PCB design software,²⁴ although the freeware version (readily

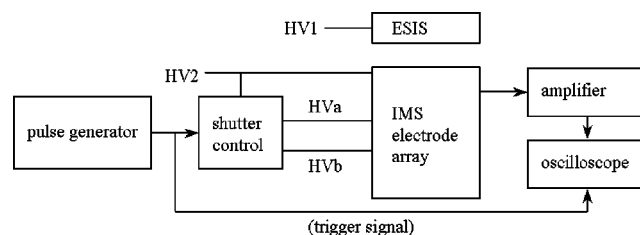


Fig. 7. Block diagram of the experimental configuration of the IMS system.

downloaded from their website²⁵) could also have been used for much of the work (the freeware version, however, has board size limitations). A PCB milling machine²⁶ was used to pattern and cut all the components of this design except for the syringe holder and Plexiglas enclosure. If such a machine is not readily available, the components, except the grids, could be made by submitting the PCB layout files to a commercial PCB manufacturing house. In our experience such manufacturing would cost approximately US\$1 per square centimeter. The IMS column could also be made from stacking conductive and insulating disks, each with a large central hole, but this would lead to more extensive condensation problems. The grids could also be made manually, given patience and sufficient dexterity.

A. Electrospray unit

For the ES ionization source (ESIS), a blunt stainless steel 27-gauge hypodermic needle was used with a 1 mL (standard laboratory) syringe as the solvent/sample reservoir. The needle tip was ground flat by a grinder and fine sandpaper. The entire ES-IMS was operated in the vertical configuration to take advantage of hydrostatic pressures to maintain liquid flow in the liquid, where a slight positive pressure was used to initially fill the syringe and initiate the formation of the Taylor cone. With our design and a tip-to-focus-grid spacing of ~ 1 cm, electrospray was initiated with potentials of 5860 and 3049 V for HV1 and HV2, as shown in Fig. 3. Note that the device was operated in the positive mode—that is, a more positive potential was applied to the ES source compared to the focus grid so as to produce positive ions in the IMS.

B. Electrode array

The electrode array was made from a stack of 61 horizontal PCB segments of the types shown in Fig. 4 that are slotted into two vertical side-boards. The average spacing between each PCB surface, i.e., between any two guard rings, was ~ 1.55 mm, while the guard ring thickness (the thickness of the conducting copper of the PCB material) was ~ 0.03 mm. This produced an IMS system with column and drift regions of length 9.65 and 5.85 cm, respectively. The drift tube inner diameter (or aperture) measured 2 cm. Each of these segments was connected to an element within the resistive divider shown in Fig. 3, where each 1 M Ω surface-mount resistor was connected in parallel with a 100 nF surface-mount ceramic capacitor.

The major steps involved in making the PCB segments were (1) milling of the “top-face” of the segments, (2) bonding of the grid material to the “top-face” of the grid segments shown in Figs. 4(b) and 4(c), (3) milling of the grid features, (4) milling of the “bottom-face” of the segments, (5) chemical (acid) etching of the grid features, and (6) coating of the tin-plate solution to protect against corrosion, i.e., oxidation.

Before engaging in the steps listed above, the ~ 1.55 mm ($\sim 1/16$ in.) thick double-sided copper-clad boards²⁷ and the milling machine had to be prepared. First, the boards were sheared to appropriate sizes for the milling process, in our case, $\sim 10 \times \sim 15$ cm (4×6 in.) and $\sim 23 \times \sim 15$ cm pieces. Utilizing the milling machine,²⁶ alignment holes were first drilled into each board using a 3.175 mm (0.1250 inch) carbide drill-bit²⁶ to facilitate the milling of both sides of the board. Prior to each milling stage, the board was placed on

top of backup material²⁶ and secured in place using 3.175 mm alignment pins and any masking/packing tape where necessary to ensure a level board.

For the first step, a 0.7874 mm (0.031 in.) stub carbide endmill²⁶ was used to route a 2-cm diameter aperture (top relief), while a 1.57 mm (0.062 in.) carbide router²⁶ was used for the perimeter of each of the 4×4 cm square PCB pieces, including the extension tabs of dimensions $\sim 11 \times 3$ mm along the width near opposing corners that will be used as the mounting struts, shown in Fig. 4, at a depth of one-third to one-half of the board’s thickness. Here, the endmill bit, which is capable of providing superior burr-free edges, was used for the more critical aperture cuts, while the less critical cuts were done with the standard router. A second pass was used to clean out the groove, followed by vacuum cleaning. For the shutter gate, the length of the PCB piece was extended by ~ 2.5 cm to accommodate the shutter gate electronics (optional).

Due to the tendency for the thin copper layer to break during the milling of the grid features, a more durable metal [in our case, brass of thickness 0.1524 mm (6/1000 in. shim stock)] was used as a substitute grid material. This second step involved (a) cleaning all the surfaces with an abrasive pad, e.g., Scotchbrite or Brillo pad; (b) marking the aperture perimeter and the outer grid perimeter onto both surfaces of the brass foil with a water-soluble marker to ensure both sides are consistent; (c) “tinning,” i.e., coating with a thin layer of solder, the top-face of the copper grid region and the bottom-face of the brass foil while avoiding the region where the aperture would be; (d) cutting and attaching the appropriately sized square pieces of brass foil to the copper layer by a process called “reflow soldering;” (e) filing away any solder spikes or bridges to avoid problems with the ceramic foot of the milling machine; and (f) cleaning with the abrasive pad. Application of a layer of rosin flux²⁷ with a cotton swab to the region surrounding the circular aperture region allowed for “tinning” a very thin layer of solder—in our case, “44@” rosin core solder,²⁸ a low-temperature, lead-containing solder. After “tinning,” the PCB grid and the brass foil were cleaned using a flux remover²⁷ applied using a paper towel. Touch-ups of the solder layers were sometimes found to be necessary at this point. The “reflow soldering” technique itself involved first placing the tinned bottom-face of the cut brass piece against the tinned copper of the PCB, with the rosin flux and solder applied (for thermal conductivity) on the top-face of the brass piece, starting near the aperture marking and pressing/squeezing outward toward the edges. This resulted in the outward seepage of the accumulated solder between the copper and brass layers, leaving a fairly flat interface. This process of reflow soldering was repeated until there were no longer any bulges due to heat deformation in the brass layer. Once again, the surfaces were cleaned with flux remover.

For the third step, the grid and shutter-gate PCB segments were aligned and secured in place on the milling machine platform. It should be noted at this point that the order of the milling process would be somewhat important considering that the delicate features of the grid that have been previously milled may be irreparably damaged by the ceramic foot (i.e., part of the solenoid activated z-stage) of the milling machine. To avoid this, one can either select the individual traces one at a time via the computer interface or attempt to preprogram the milling order by anticipating the system software. For the grid features, the stub endmill was

again used to mill out the features at a depth of ~ 0.2 mm (8/1000 in.) with a typical feed-rate of ~ 38 cm/min (15 in./min).

For the fourth step, masking tape was first applied over the already milled top-face of the boards to prevent the pieces from moving freely as they are cut loose from the parent board; this prevents the pieces from being damaged or even jamming the milling machine. The boards were then flipped and secured in place. The first step was repeated at a depth that allowed the stub endmill and router bits to exit through the groove on the (presently face-down) top-face so that the various pieces, i.e., the extraneous center pieces, the grids and the guard rings, would fall out individually if not for the masking tape holding them in place. For the grids and the shutter gate, the extraneous center pieces were held down carefully during routing to facilitate the cut but not to damage the grid features beneath.

For the fifth step, the individual grids and shutter gate pieces were chemically (acid) etched to remove the burrs on the grids left by the milling process. The pieces were pre-rinsed with distilled water, then submerged face-down (grid-side-down) in approximately 100 mL of water held in a Pyrex glass container. Approximately 50 mL of 5 M concentration nitric acid²⁹ was then poured around each PCB grid piece so that the acid would rise through the features of the grid. (CAUTION: Handling of acids requires the use of appropriate safety equipment, i.e., gloves, apron, face shield, ventilation, etc., and proper disposal methods when done.) Once the burrs had been removed, as determined by periodic visual inspection, the Pyrex container was emptied of acid and rinsed with water to stop the etching process. The grids were then washed under running water. An abrasive pad was used to clean the discolored grid surfaces; discoloration is due to the interaction of the acid with the lead in the solder. Any remaining burrs were removed with the use of 240 sandpaper, although a finer grain would be even better. Alternative methods of constructing the shutter gate have been reported.^{13,23,30}

For the sixth step, all the milled pieces were cleaned once more with the abrasive pad to remove any edges from the IMS column pieces, but more importantly to remove any surface oils. Once done, the various pieces were submerged for several minutes in liquid tin²⁷ primarily to protect against oxidation.

After the individual pieces were constructed, the IMS column (or drift tube) was assembled by sandwiching the grids, the guard rings, and the shutter gate between the two single-sided, slotted side-boards in which the tabs of each PCB segment would fit. Solder was applied to secure the pieces in place to create a rigid structure where the electric field uniformity in the drift region could be maintained.

C. High voltage switch circuit

The high voltage switch produces the voltages to control the shutter gate. As shown in Fig. 5, one output line, HVa, is constant at a potential HVx and the other, HVb, is switched between the potentials HVx and HVy using the two high voltage phototransistor optocouplers³¹ shown in the circuit of Fig. 5. Both HVx and HVy are produced from the voltage divider shown in Fig. 5, with $HVx = 3 \text{ kV} \times (\frac{37}{61}) = 1.82 \text{ kV}$ and $HVy = 3 \text{ kV} \times (\frac{36}{61}) = 1.77 \text{ kV}$. With a “high” input to the

circuit the HVb output is 1.82 kV, and with a “low” input the HVb output is 1.77 kV. In either case the HVa output remains at 1.82 kV.

The addition of the resistor between pins 1 and 6 of OK1 in the circuit of Fig. 5 allows a more rapid turn-off of the attached optocoupler ($\sim 131.9 \mu\text{s}/0.8 \mu\text{s}$, fall/rise time ratio). The turn-on time was far faster. The minimum gate open time was dictated by these transition times but was comparable with values reported, i.e., 0.2 ms^{32–34} to 0.5 ms,^{35,36} for systems with more complex voltage pulsers.

D. Transconductance amplifier

The input of the detector circuit shown in Fig. 6 was tied to the collector plate and was designed to have a gain of $1.01 \times 10^9 \text{ V/A}$; the measured rise time was 1 μs . This circuit was based upon the design suggested in Ref. 37, a design that is remarkable for its high speed of operation and great sensitivity. In building this circuit, great care had to be taken so as not to introduce leakage paths on circuitry from the detector plate to the input of the op-amp; this connection was made by using a Teflon-insulated feed-thru,³⁸ and a “flying wire” connection.³⁹ We cleaned the PCB with alcohol and wore gloves when assembling the circuit in order to avoid contaminating the PCB surface. High (HF, \sim few kHz) and low frequency (LF, $\sim 60 \text{ Hz}$) noise measurements were made without any efforts to shield against electromagnetic interference and without any noise filters, where $\sim 150 \text{ mV}$ peak-to-peak LF and $\sim 50 \text{ mV}$ peak-to-peak HF noise was detected with the input to the amplifier of Fig. 6 open-circuited. During the experiments, the input, i.e., the collector plate, was partially shielded by the column, yielding $\sim 50 \text{ mV}$ peak-to-peak LF noise, before averaging. Averaging over 512 scans reduced this noise considerably, resulting in noise amplitudes of $\sim 2 \text{ mV}$ peak-to-peak.

IV. MODIFICATIONS

We used two 0–6 kV positive high voltage power supplies⁴⁰ whose output voltages are controlled by a 0–5 V analog input signal. To set the voltage of the high voltage power supplies as well as setting the timing for the shutter gate, a circuit based upon a PIC microcontroller⁴¹ was used. This circuit included an analog-to-digital converter device (ADC) and a digital-to-analog converter (DAC) device. These devices were controlled by the microcontroller. This hardware used the DACs to set the high voltages and could use the ADC to acquire the data. In the future we intend to have this microcontroller manage the data acquisition, thereby removing the need for the oscilloscope and potentially making this a hand-held system. We expect that most users of this system will simply use off-the-shelf high voltage supplies—the complexity of the microcontroller system is not warranted unless needed for more advanced integrations.

V. DEMONSTRATION

Electrospray was produced upon loading the syringe with a solution of 50% methanol and 50% distilled and de-ionized water, and applying 5.86 kV to the needle and 3 kV to the focus grid. The solution prepared from autoclaved and 0.45 mm filtered Milli-Q de-ionized and distilled water and 100% methanol²⁹ was mixed without additional modifications. It was then observed that the shutter signal controlled the pas-

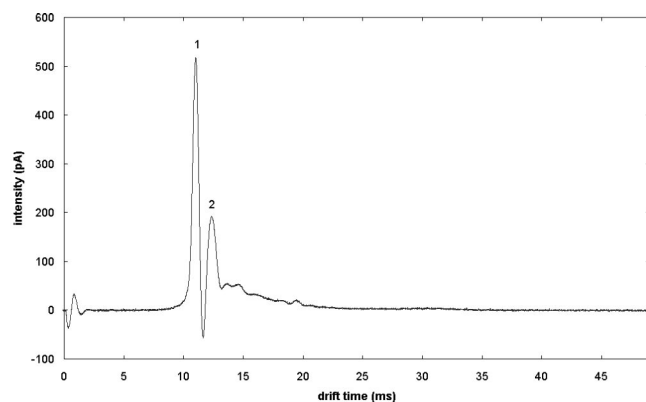


Fig. 8. Ion mobility spectrum of 50:50 (v/v) methanol/water. The drift length, voltage, temperature, and pressure were 5.85 cm, ~ 1820 V, $\sim 20^\circ\text{C}$, and ~ 710 Torr, respectively. The reduced mobilities (K_o) for peaks 1 (methanol) and 2 (water) are 1.48 and $1.32\text{ cm}^2 (\text{V s})^{-1}$, respectively.

sage of ions reaching the detection plate and hence the current delivered to the detector. The system has considerable similarity to a vacuum tube triode. This arrangement produces a drift field of $\sim 310\text{ V/cm}$ with a pulse width of ~ 0.3 ms at a drift tube temperature of $\sim 20^\circ\text{C}$.

At this point the system was attached, as shown in Fig. 7, to a 20 Hz control signal with a 0.2% positive duty cycle that was used to trigger the oscilloscope. To improve our signal-to-noise ratio, the oscilloscope was used to average 512 consecutive runs, i.e., over 25.6 s.

Figure 8 depicts the ion mobility spectrum obtained by this system with this methanol/water sample, showing two main peaks labeled 1 and 2. This spectrum is remarkably similar to that of Hill and co-workers³² and by comparison we attribute peak 1 to methanol, and peak 2 to water. In other work in the literature, e.g., Hill *et al.*,³² the assignment of the identity of the peaks is typically done with a MS. Due to the high surface tension of the water, it is not possible to electrospray water alone without modifications to the system or the electrospray source; we have encountered this problem as have others.⁴² The first few milliseconds of the trace in Fig. 8 show an undulation which is associated with the switching of the shutter gate; the capacitors shown in Fig. 3 and the separate resistor array shown in Fig. 5 help minimize this effect. This undulation was present when runs were made without a sample present (data not shown). The later (weak) peaks seen in Fig. 8 are not attributed to any particular component, as they are not always present. Hill and co-workers also observed these “bumps,” although they did not speculate as to their identity.³² They may be from ions produced from the air around the tip of the Taylor cone via corona ionization.

IMS spectra are commonly described in terms of reduced mobility values K_o given by

$$K_o = [L^2 / (t_d V)] (273.15\text{ K} / T) (P / 760\text{ Torr}), \quad (1)$$

where $L = 5.85\text{ cm}$, $V = 1820\text{ V}$, $T = 293.15\text{ K}$, and $P = 710\text{ Torr}$ are the drift length, voltage, temperature, and pressure, respectively; the 11.0 and 12.4 ms drift times, t_d , of the two solvent peaks correspond to reduced mobilities of 1.48 and $1.32\text{ cm}^2 (\text{V s})^{-1}$, respectively. These values are somewhat similar to those of the Hill group,³² who obtained values of 1.95 and $1.82\text{ cm}^2 (\text{V s})^{-1}$,⁴³ although it is difficult to compare values between dissimilar systems, especially

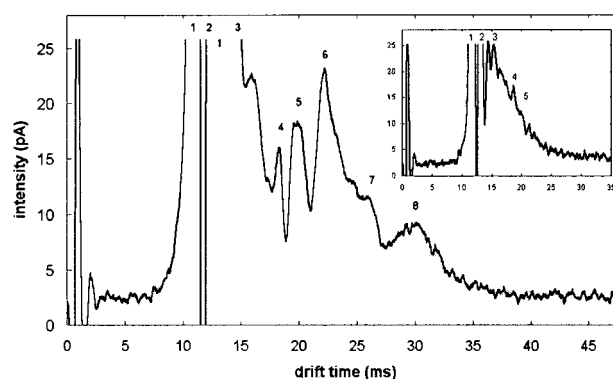


Fig. 9. Ion mobility spectrum of cytochrome c (1 mg/mL concentration) compared with a 50:50 (v/v) methanol/water solvent spectrum (inset). Peaks 6–8 are due entirely to the cytochrome c, while peaks 1 and 2 are due to solvent peaks, and peaks 3–5 are due to possible air contaminants.

where different drift gases and temperatures are utilized.

The peak resolution, a quantity indicative of the ability of any spectrometer to distinguish between two closely spaced peaks, is given by $R_p = t_d / w_{1/2}$, with $w_{1/2}$ as the temporal-width at half-height and t_d the peak arrival time. The peak resolution values were found to be 19.37 and 14.6, respectively, for peaks 1 and 2. These values are also comparable to those of Hill and co-workers, whose values, obtained from Fig. 2 of Ref. 32, are 23, 18, and 19, respectively, for their three peaks. It is surprising that we were able to obtain similar resolution given that their experiments were made with significantly more complex systems involving high temperatures, drift gases, syringe pumps, etc., and with longer drift columns.

These results show only the spectra of the carrier solvents, methanol and water, at concentrations of 50%. When a small concentration of a protein is added, the many ionization states, e.g., $+12$ – $+18$,³⁶ and the ease of ionization of such a species relative to water and methanol produces a very large contribution to the ion current, thereby making the instrument more sensitive to the detection of such species. In more recent work with the protein cytochrome c at a concentration of 1 mg/mL^{44,45} we have obtained a limit of detection (LOD) of $\sim 100\text{ }\mu\text{g/mL}$ or $\sim 100\text{ ppm}$. With a molecular weight of $12\,327\text{ g/mol}$ for cytochrome c, this LOD corresponds to $8 \times 10^{-6}\text{ M}$. Although LOD values are frequently not specified in the literature (we have not encountered any for cytochrome c), one example of an LOD is $7.5 \times 10^{-7}\text{ M}$ for atrazine,⁴⁶ a value that was obtained using an ES-based IMS of significantly greater complexity. An ion mobility spectrum of 1 mg/mL cytochrome c is shown in Fig. 9, with a solvent-only spectrum for comparison shown in the inset of the figure. Peaks 1 and 2 were identified above, and peaks 3–5 are likely air contaminants as described above. Peaks 6–8 are due to the cytochrome c.

VI. CONCLUSIONS

This device is an interesting and low cost system that could be fabricated using the electronics and PCB construction equipment that can be found in many undergraduate laboratories or even well-equipped high school laboratories. Despite this simplicity the system does serve to demonstrate the production of ions from a liquid sample as well as measuring their time-of-flight. Although the system does not in-

volve the many additional features of the standard systems described in the literature, we have obtained results comparable to those systems. The present system could be built by an experienced PCB technician in several days for the first system, and considerably less time for any further copies.

Apart from the high voltage power supplies and the Plexiglas enclosure, the main cost of the system is that of the PCB material. In future work we intend to move to the use of HV supplies based on the "Lightning" supplies of Doty *et al.*,⁴⁷ however, with a maximum current that we would set in the microampere range to ensure safe use. There is some difficulty with loading the sample within the present system—one wishes to fill the needle to the tip without forcing, i.e., "pumping" the liquid into the system. "Pumping" inevitably leads to the accumulation of large droplets on the focus grid. However, this is sometimes unavoidable, thus requiring anywhere from 5 to 15 min for the spray to settle resulting in a "clean" spectrum. Once stable electrospray has been achieved we have performed many thousands of runs over the course of several hours from a single sample loading of less than 100 μL , where the spectra remained unchanged during this stable state.

We believe that this system provides a good foundation for demonstration, experimentation, and development. A wide variety of samples could be analyzed, suggesting the possible use of this system in conjunction with a biotechnology demonstration. This system also could be a good basis for projects developing advanced signal-processing methods or low-noise circuit design.

VII. DISCLAIMER

Despite having made every effort to build a safe system, great care should be exercised when using any instrument based on the use of high voltages. Appropriate care should also be taken, e.g., protective gear should be worn, when handling chemicals and biological samples.

ACKNOWLEDGMENTS

We gratefully acknowledge the support of the Natural Sciences and Engineering Research Council of Canada. We also greatly appreciate the assistance and flexible schedule of Edward Tiong, a laboratory technician within our department.

^aAuthor to whom correspondence should be addressed. Electronic mail: chrisb@ee.ualberta.ca

¹D. C. Collins and M. L. Lee, "Electrospray ionization gas-phase electrophoresis under ambient conditions and its potential or high-speed separations," *Fresenius' J. Anal. Chem.* **369** (3-4), 225–233 (2001).

²L. W. Beegle, I. Kanik, L. Matz *et al.*, "Effects of drift-gas polarizability on glycine peptides in ion mobility spectrometry," *Int. J. Mass. Spectrom.* **216** (3), 257–268 (2002).

³I. Kanik, L. W. Beegle, and H. H. Hill, "Ultra high-resolution electrospray ionization/ion mobility spectrometer system for in-situ detection of organic compounds," presented at the Conference of Lunar and Planetary Science, Lunar and Planetary Institute, Houston, TX, 2001 (unpublished).

⁴C. A. Srebalus, J. W. Li, W. S. Marshall *et al.*, "Gas phase separations of electrosprayed peptide libraries," *Anal. Chem.* **71** (18), 3918–3927 (1999).

⁵R. Guevremont, K. W. M. Siu, J. Y. Wang *et al.*, "Combined ion mobility time-of-flight mass spectrometry study of electrospray-generated ions," *Anal. Chem.* **69** (19), 3959–3965 (1997).

⁶Smiths Detection, Smiths Group plc (London, UK), 2002, website: <http://www.smithsdetection.com/Products/>.

⁷GE Industrial Systems (Plainville, CT), General Electric Company, 2003, website: <http://www.geindustrial.com/ge-interlogix/iontrack/index.html>.

⁸J. P. Carrico, D. W. Sickenberger, G. E. Spangler *et al.*, "Simple electrode

design for ion mobility spectrometer," *J. Phys. E* **16** (11), 1058–1062 (1983).

⁹G. A. Eiceman, D. A. Blyth, D. B. Shoff *et al.*, "Screening of solid commercial pharmaceuticals using ion mobility spectrometry," *Anal. Chem.* **62** (14), 1374–1379 (1990).

¹⁰G. A. Eiceman, "Advances in ion mobility spectrometry-1980–1990," *Crit. Rev. Anal. Chem.* **22** (1-2), 17–36 (1991).

¹¹Gary Alan Eiceman and Zeev Karpas, *Ion Mobility Spectrometry* (CRC, Ann Arbor, 1994).

¹²O. Soppart and J. I. Baumbach, "Comparison of electric fields within drift tubes for ion mobility spectrometry," *Meas. Sci. Technol.* **11** (10), 1473–1479 (2000).

¹³G. E. Spangler, "Theory and technique for measuring mobility using ion mobility spectrometry," *Anal. Chem.* **65** (21), 3010–3014 (1993).

¹⁴L. M. Matz, B. H. Clowers, W. E. Steiner *et al.*, "Liquid-sheath-flow electrospray ionization feasibility study of direct water analysis with the use of high-resolution ion-mobility spectrometry," *Field Anal. Chem. Technol.* **5** (1-2), 91–96 (2001).

¹⁵C. Wu, W. F. Siems, and H. H. Hill, "Secondary electrospray ionization ion mobility spectrometry/mass spectrometry of illicit drugs," *Anal. Chem.* **72** (2), 396–403 (2000).

¹⁶L. M. Matz, W. E. Steiner, B. H. Clowers *et al.*, "Evaluation of micro-electrospray ionization with ion mobility spectrometry/mass spectrometry," *Int. J. Mass. Spectrom.* **213** (2-3), 191–202 (2002).

¹⁷G. R. Asbury, J. Klasmeier, and H. H. Hill, "Analysis of explosives using electrospray ionization/ion mobility spectrometry (ESI/IMS)," *Talanta* **50** (6), 1291–1298 (2000).

¹⁸G. K. Batchelor, *The Scientific Papers of Sir Geoffrey Ingram Taylor* (The Syndics of the Cambridge U.P., Cambridge, 1971), Vol. 4.

¹⁹M. Cloupeau, "Recipes for use of EHD spraying in cone-jet mode and notes on corona discharge effects," *J. Aerosol Sci.* **25** (6), 1143–1157 (1994).

²⁰J. F. de la Mora and A. Gomez, "Remarks on the paper 'Generation of micron-sized droplets from the Taylor cone,'" *J. Aerosol Sci.* **24** (5), 691–695 (1993).

²¹P. Kebabian, "A brief overview of the present status of the mechanisms involved in electrospray mass spectrometry," *J. Mass Spectrom.* **35** (7), 804–817 (2000).

²²P. Kebabian and L. Tang, "From ions in solution to ions in the gas-phase—the mechanism of electrospray mass-spectrometry," *Anal. Chem.* **65** (22), A972–A986 (1993).

²³Norris E. Bradbury and Russell A. Nielsen, "Absolute values of the electron mobility in hydrogen," *Phys. Rev.* **49**, 388–393 (1936).

²⁴Eagle PCB design software available from CadSoft Computer, Inc., Delray Beach, FL.

²⁵CadSoft Computer, Inc. (Delray Beach, FL, USA), 2002, website: <http://www.cadsoftusa.com/>.

²⁶Quick circuit 5000, DB-1250 carbide drill-bit, EM-0310-2S stub carbide endmill, CR-0620-R2 carbide router, and Backup Material available from T-Tech, Inc., Atlanta, GA.

²⁷Cat. No. 555 copper-clad board, 835-100ml no clean rosin flux, 4140-400G flux remover for PC boards, and 421-500ML liquid tin available from MG Chemicals, Toronto, ON, Canada.

²⁸24-6337-0023 rosin core solder available from Kester, Chicago, IL.

²⁹Nitric acid and A408-1 certified ACS spectranalyzed (100%) methanol available from Fisher Scientific Ltd., Nepean, ON, Canada.

³⁰David J. Nowak, James E. Rice, and Donald R. Bianco, "Ion gating grid," United States Patent No. 4,150,319 (17 April 1979).

³¹H11D1 phototransistor optocoupler available from Fairchild Semiconductor, South Portland, ME.

³²Y. H. Chen, W. F. Siems, and H. H. Hill, "Fourier transform electrospray ion mobility spectrometry," *Anal. Chim. Acta* **334** (1-2), 75–84 (1996).

³³C. Wu, W. F. Siems, G. R. Asbury *et al.*, "Electrospray ionization high-resolution ion mobility spectrometry-mass spectrometry," *Anal. Chem.* **70** (23), 4929–4938 (1998).

³⁴C. Wu, W. F. Siems, J. Klasmeier *et al.*, "Separation of isomeric peptides using electrospray ionization/high-resolution ion mobility spectrometry," *Anal. Chem.* **72** (2), 391–395 (2000).

³⁵D. Wittmer, B. K. Luckenbill, H. H. Hill *et al.*, "Electrospray-ionization ion mobility spectrometry," *Anal. Chem.* **66** (14), 2348–2355 (1994).

³⁶Y. H. Chen, H. H. Hill, and D. P. Wittmer, "Thermal effects on electrospray ionization ion mobility spectrometry," *Int. J. Mass Spectrom. Ion Processes* **154** (1-2), 1–13 (1996).

³⁷Joseph F. Keithley, *Low Level Measurements: Precision dc Current, Volt-*

- age and Resistance Measurements, edited by John Yeager and Mary Anne Hrusch-Tupta (Keithley Instruments, Cleveland, 1998).
- ³⁸Teflon-insulated feed-thru available from Wearnes Cambion Ltd., Hope Valley, Derbyshire, UK.
- ³⁹An example of the “flying wire” connection also referred to as “air wiring” can be found in the datasheet for the “precision CMOS dual micropower operational amplifier” (LMC6062; National Semiconductor).
- ⁴⁰C60 6 kV positive high voltage supply available from EMCO High Voltage Corporation, Sutter Creek, CA.
- ⁴¹PIC16F877 microcontroller available from Microchip Technology Inc., Chandler, AZ.
- ⁴²K. Q. Tang and A. Gomez, “Generation of monodisperse water droplets from electrosprays in a corona-assisted cone-jet mode,” *J. Colloid Interface Sci.* **175** (2), 326–332 (1995).

- ⁴³These values of reduced mobilities were calculated, by us, from the parameters listed and the drift times from the spectrum found in Ref. 32.
- ⁴⁴C3131 bovine heart cytochrome c available from Sigma-Aldrich.
- ⁴⁵E. C. S. Cheong, “Electrospray ionization for applications in ion mobility spectrometry,” MSc. thesis, University of Alberta, 2003.
- ⁴⁶C. Wu, H. H. Hill, and A. P. Gamedinger, “Electrospray ionization ion mobility spectrometry as a field monitoring method for the detection of atrazine in natural water,” *Field Anal. Chem. Technol.* **2** (3), 155–161 (1998).
- ⁴⁷S. D. Doty, M. Craggs, M. Jorgensen *et al.*, “The ‘lightning machine’: A simple interesting demonstration apparatus for introductory physics,” *Am. J. Phys.* **68** (6), 579–581 (2000).

Realization of an optical profiler: Introduction to scanning probe microscopy

J.-M. Friedt^{a)}

IMEC, Kapeldreef 75, 3001 Leuven, Belgium

(Received 7 January 2003; accepted 19 December 2003)

Scanning probe microscopy is a widely used instrumentation method based on scanning a probe over a sample to map the spatial variation of a physical property over its surface. Here we present the steps required for the realization of a generic scanning probe microscope. The selected sensor is a CD reader optical head that monitors the distance to the focusing point of a lens by which an infrared laser is focused on the reflecting surface of the sample. We thus develop an optical profiler and illustrate practical examples by mapping the topography of a coin. The focus of this article is to describe a low cost profiler illustrating all the steps of the development, from the definition of the probe of the physical property to be monitored to the result on an actual sample. © 2004 American Association of Physics Teachers.

[DOI: 10.1119/1.1648329]

I. INTRODUCTION

Scanning probe microscopies (SPM) are used in an ever wider range of applications, from material science to biology, probing surfaces at the micrometer, nanometers, and atomic scale depending on the probe. Here we propose to tackle this subject from an experimental point of view by realizing an optical profiler that works by following a principle similar to a SPM and that requires solving the same problems as the ones encountered during the development of a SPM.

As opposed to more familiar imaging sensors such as the eye or a camera in which a large number of identical sensors work in parallel (in this example, light intensity sensors), a scanning probe microscope¹ scans a probe over a large number of distinct points in space and thus maps the spatial distribution of the physical property being analyzed. This property can be the probe–sample distance (e.g., using the tunneling current^{2–6} or the force applied to a tip⁷), the local magnetic field,⁸ the electrochemical current,⁹ the thermal conductivity, etc.

A functional scanning probe microscope requires the solution of the following three problems:

- (1) obtaining a probe–surface distance sensor with a bijectivity range as wide as possible and a noise level as low as possible in order to achieve a good vertical resolution—throughout this document bijectivity will mean that we can find a range in the probe–sample dis-

tance for which a unique measurement is obtained for a given distance, and this measurement is a unique representative of that distance;

- (2) obtaining a precise positioning of the sample relative to the probe in the scanning plane;
- (3) software able to move the sample relative to the probe, and for each new position read the probe–surface distance.

We will describe these steps in the realization of a profiler whose basic working principle is similar to that of the atomic force microscope (AFM). The main analysis focuses on the use of the optical head of a laser compact-disc (CD) reader^{10,11} as a probe–surface distance sensor (where the probe is the lens focusing the laser). The positioning of the sample is achieved by fixing it on a digitally controlled plotter, while the software controls the various parts of the instrument.

The chronology of the development is thus the following:

- (1) confirm the working condition of the optical head taken from a broken CD reader; identify the laser diode pinout and understand how to power it (Sec. II);
- (2) power the laser diode properly for a stable, long term use (Sec. II A) by using the feedback of the emitted light power on the power supply voltage;
- (3) detect the signal related to the distance between the focal point of the laser and the reflecting surface of the sample (Sec. II B);

- (4) power the electromagnet to which the laser focusing lens is attached in order to be able to vary the probe–surface distance;
- (5) accurately position the sample under the probe in order to be able to image the topography of the surface (Sec. III).

II. THE CD READER OPTICAL HEAD

The use of a CD reader optical head is an interesting, compact, and low cost option for the development of sensors requiring a light source and photodetectors (see, for example, the development of a DNA-chip¹² based on such a component).

The CD reader optical head includes a laser diode emitting in the near infrared, around 780 nm; a lens attached to a coil used as an electromagnet for varying the vertical position of the lens by varying the current flowing in the coil, as shown in Fig. 1; a four-quadrant photodetector whose signal, after proper signal processing, provides a bijective relationship with the lens–surface distance.

Following the data provided by the optical head manufacturers, the laser spot reflected from the surface after focusing by the mobile convergent lens is characterized by a diameter in the micrometer range, in our case 1.7 μm .

Since we are going to use the various parts of the optical head to construct the profiler, a good understanding of the way each part works—the power supply of the laser diode, the photodiodes, and the electromagnet coil—is required.

A. Laser power supply

The laser diode includes an emitting part and an integrated photodetector which provides an electrical signal that is a function of the emitted power (Fig. 2). Considering that the impedance of the emitting diode decreases with temperature and that the emitted power increases with the current flowing through its junctions, a constant voltage power supply would quickly lead to the destruction of the diode.

We must therefore develop an output-power controlled power supply, as shown in Fig. 3. We have achieved this result by using an operational amplifier whose stabilizing feedback loop between the output and the inverting input compares the voltage output of the integrated photodetector (which is a function of the emitted power) with a setpoint voltage. If the emitted light power is too great, the voltage obtained from the photodetector is greater than the setpoint voltage and the difference between the voltages at the inverting input V_- and the noninverting input V_+ of the operational amplifier becomes negative, $\varepsilon = V_+ - V_- < 0$, and the output voltage of the operational amplifier decreases. The opposite argument shows that if the emitted power is insufficient, the supply voltage and thus the output current of the operational amplifier increase.

The diode begins emitting laser light when the supply current reaches a value around 60 mA, as shown in Figs. 2 and 3(a). Such a current cannot be provided directly by an operational amplifier; a transistor wired in a current-amplifier configuration must be added to the output of the operational amplifier. We have chosen to use a 2N3055 power transistor, greatly oversized, in order to avoid problems related to heating that have been observed with smaller transistors. The laser power supply circuit must indeed be able to provide a stable output over several hours. Including the transistor in

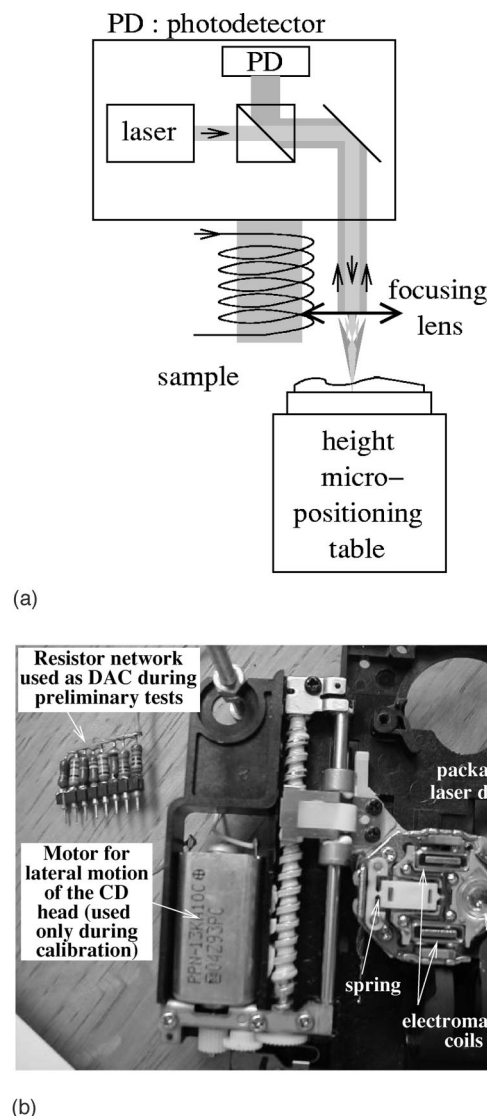
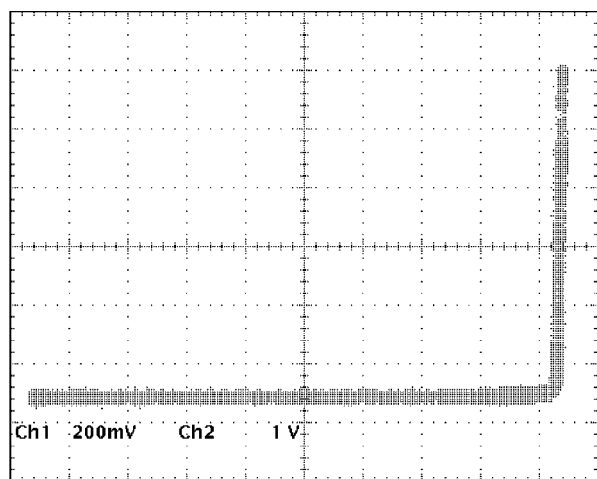


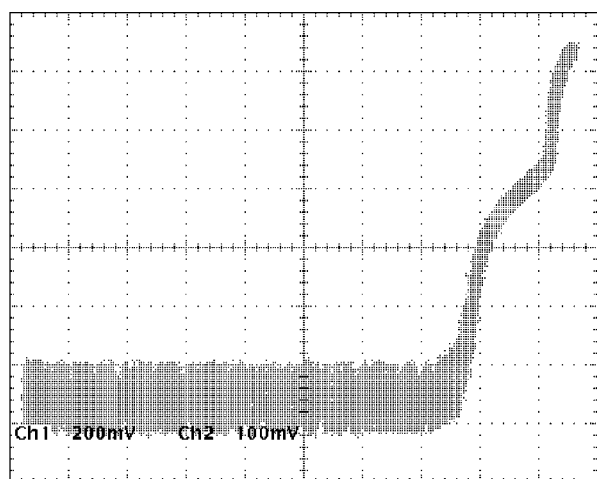
Fig. 1. (a) Diagram of the CD reader optical head: the distance between the lens and the sample can be adjusted by varying the current flowing in the coil of the electromagnet to which the focusing lens is fixed. A four-quadrant photodetector sends back an electrical signal which is a function of the distance between the focal point of the lens and the reflecting surface of the sample. (b) Photograph of one of the CD heads used during the development of this project. The motor used for positioning the head over the disc is used for the calibration as shown in Fig. 5, while the head is kept at a fixed position and the sample is scanned in mapping experiments.

the feedback loop of the operational amplifier does not change the principle of the laser diode power supply circuit.

The setpoint voltage required for reaching a reasonable emitted light power is obtained by *briefly* supplying the diode with an ideal voltage source through a resistor of a few hundred ohms. The light intensity emitted by the diode is first monitored using an external photodiode located under the lens of the CD reader head. A CCD sensor from a webcam can also be used for this operation if the eventual blue filter has first been removed: this filter is sometimes used to avoid saturation of the sensor by infrared sources during normal uses. Once the laser emission has been observed by the external photodiode, the voltage coming from the integrated photodetector is monitored while increasing the laser diode supply voltage: write down the value read from the photode-



(a)



(b)

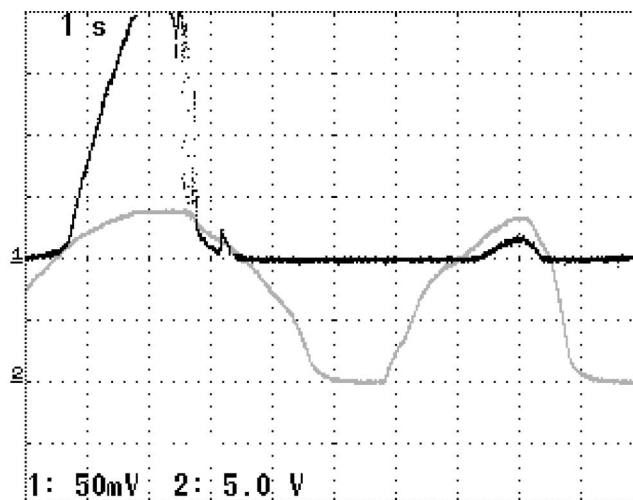
Fig. 2. (a) Intensity observed by an external photodiode located under the focusing lens, as a function of the supply voltage, and (b) photodetector response as a function of the supply voltage. In both cases the abscissa depicts the supply voltage applied through a 100- Ω resistor to pin 1 of the laser diode as shown in Fig. 3 at a scale of 200 mV/division. The ordinates display (a) the voltage at the output of a Hamamatsu S3399 silicon diode at a vertical scale of 1 V/division and (b) the output of the photodetector integrated to the laser diode for monitoring the emitted intensity at a scale of 100 mV/division.

tector when the laser emission is clearly visible on the external photodiode. This will be the setpoint voltage to be used in the circuit described previously.

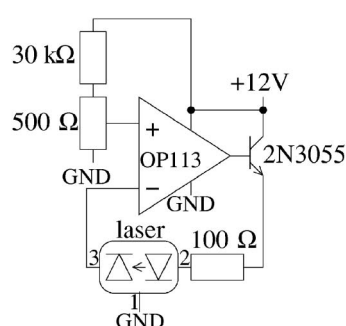
The pinout of all laser diodes tested during the development of this experiment were the same as shown in Fig. 3(c). Be aware that any error in the initial connection of the laser diode will most certainly lead to its immediate destruction.

B. Using the reception photodiode quadrant

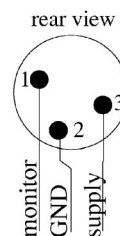
Let us remind ourselves of the working principle of a CD head in disc-reading mode. When used for reading a disc, the photodiode quadrant integrated in the CD reader head works in the following way. A four-quadrant receiving area monitors the focusing of the laser spot on the reflecting surface, and two photodetectors located on both sides of the four-quadrants sensor are used to keep the head located over the track being read.



(a)



(b)



(c)

Fig. 3. (a) Laser power emitted as a function of the supply voltage applied through a 100- Ω resistor: the gray (bottom) trace is the supply voltage as a function of time depicted with an abscissa scale of 1 s/division and a vertical scale of 5 V/division. The black (top) trace is the emitted power as observed by a silicon diode Hamamatsu S3399 located under the focusing lens. Notice the fast rise of the emitted intensity when the threshold current value of around 60 mA is reached. (b) Electronic power supply circuit designed for keeping constant the emitted light intensity. The purpose of this circuit is to tune the voltage output of an OP113 op-amp (which actually is a quarter of an OP413 quad-op-amp) so that the signal read from the laser diode internal photodetector is equal to the setpoint voltage provided on the noninverting pin. The voltage at the emitter of the power transistor is measured to be around 6 V when the feedback is working properly. (c) Pinout of the laser diode, using the same pin numbering as in (b).

All photodiodes are polarized by a +5 V voltage in order to improve their response speed to a frequency of a few megahertz. Remember that 74 min of music must fit on a 650-Mbyte disc, leading to a required bandwidth of at least 1.2 Mbytes/s \sim 1.2 MHz.

The intensity of the light hitting the photodetectors modulates the conductivity of the photodiodes and hence varies the voltage output of the polarized photodiodes. The circuit presented in Fig. 4(a) converts the voltages W_j from the photodiodes to currents through the resistors Q_j . These currents are summed at the noninverting input V_+ and the resistor Q acts as a current to voltage converter. Finally, the op-amp converts the high-impedance input voltage V_+ to a low impedance output voltage S through the follower circuit using the resistor R (which might eventually be equal to 0). A formal analysis of the circuit using Millman theorem

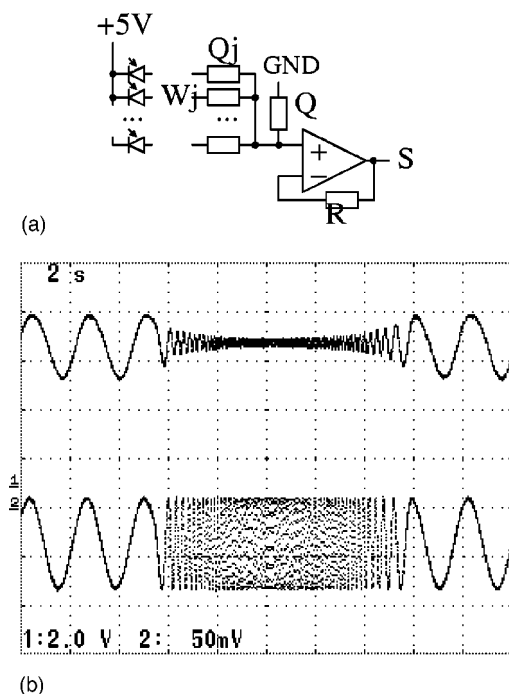


Fig. 4. (a) Circuit used to combine the signals coming from the multi-quadrant photodetector (depicted as “PD” in Fig. 1 and symbolized here by the photodiodes defining the voltages W_j) after reflection of the laser on the surface of the sample. The summation of the voltages is achieved by the resistors Q_j acting as voltage to current converters and adders, and the result is converted back to a voltage by the resistor Q . The gain of the adder is set by the feedback resistor R . This output voltage is read by an analog-to-digital converter for further processing. (b) Evolution of the signal obtained after summing the currents from the four photodiodes in the CD reader head (bottom: abscissa scale is 2 s/division, vertical scale is 50 mV/division) as a function of the frequency of the voltage driving the electromagnet (top: abscissa scale is 2 s/division, vertical scale is 2 V/division) controlling the position of the lens relative to the sample. Such a curve provides an estimate of the bandwidth of about 10 Hz and hence of the response time of the CD reader head when used in a closed loop configuration.

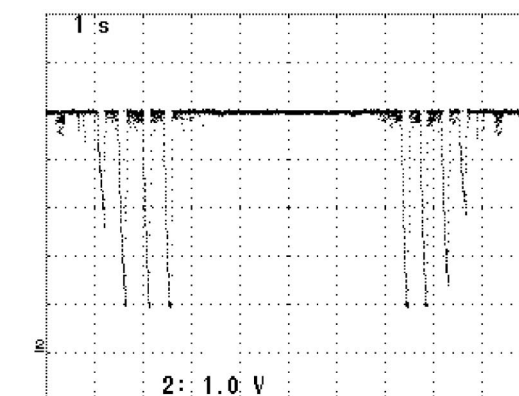
shows that the voltage output S is given as a function of the voltage inputs W_j as defined by the photodetectors by

$$\frac{S}{R} = \frac{\frac{1}{R}}{\frac{1}{Q} + \sum_{j=1}^J \frac{1}{Q_j}} \left(\sum_{j=1}^J \frac{W_j}{Q_j} \right). \quad (1)$$

By assuming that all resistors are chosen with the same value, i.e., that $R = Q = Q_j$, this expression is simplified to

$$S = \frac{1}{J+1} \sum_{j=1}^J W_j. \quad (2)$$

We check that this circuit indeed sums the intensities read from the diodes. However, as opposed to the purpose for which the photodetector quadrant was designed in which the astigmatism of the focusing lens is used to generate patterns on the photodetectors characteristic of the distance of the focus point to the surface of the sample, we here simply sum the signals obtained from the diodes. One should theoretically add the signals from diagonally opposed diodes, and subtract the resulting two signals, but it was observed experimentally that a sum of all the signals provided better results.



(a)



(b)

Fig. 5. (a) Display of the sum of the signals read from the four-quadrant photodiode of the CD reader head when a brass sample in which grooves of increasing depth, first with unknown depth and then from 100 to 500 μm with 100 μm steps, have been milled is scanned. This measurement provides an idea on the working range of the sensor: the signal saturates when the groove depth is greater than 300 μm , while the 100- to 300- μm -deep grooves are well resolved. (b) Photograph of the milled brass sample used for calibration: the width of the grooves is 2 mm. The scan was made from left to right and right to left, in a direction normal to the axis of the grooves.

Although we have illustrated Eq. (1) by taking $Q_j = Q$ to make it easier to interpret, we have actually chosen $Q \gg Q_j$ so that the sum of the currents is converted to a voltage high enough to be usable: we have used $Q = 1 \text{ M}\Omega$ and $Q_j = 560 \Omega$ in our circuit.

A signal that is a function of the lens-sample distance is thus generated as shown in Fig. 4(b).

C. Estimate of the working range of the sensor

A first quick analysis using the dc motor that controls the lateral position of the CD reader head shows that the open-loop measurement range as obtained by only reading the signal output from the photodiodes without feedback control of the lens-sample distance is quite restricted, of a few hundreds of microns at most. The graph presented in Fig. 5 demonstrates that the laser diode-photodetector quadrant set is working properly.

III. THE PLOTTER

Once the vertical distance sensor has been installed and calibrated, a second issue related to the lateral displacement of the sample relative to the probe arises. This part can be

made independent of the previous one by keeping the probe fixed and by translating the sample. This option is the one used in many implementations of the AFM since it decouples the horizontal positioning of the sample and vertical positioning of the probe.

We have in this setup used a second-hand plotter, a Roland DXY-1200, which provides a lateral resolution of 25 μm and can be digitally controlled with an RS232 serial link at 9600 baud. The language used to control the plotter, HPGL, is well documented and easy to use.¹³ This solution is easier to implement than using an analog plotter¹ which requires two additional digital-to-analog converters and does not guarantee a constant lateral resolution.

The only HPGL commands useful in this application are PU; for raising the pen-holder (and hence bring the sample to a pre-defined height), PAx, y to bring the sample to the position (x,y) preliminarily defined where the CD reader head was positioned, and finally PRx, y; to move the sample a distance (x,y) relative to its current position. This latter command is used with the sets ($\pm 1, 0$) during a line scan with a 25 μm /pixel resolution and (0, 1) to switch to the next line. All the x and y values are in units of 25 μm /pixel.

IV. THE SOFTWARE

We identify two modes for using an AFM which we call open loop and closed loop operations. In the former, the probe is positioned at the beginning of the scan at a given distance from the surface of the sample where the signal-distance function displays a maximum slope in a bijectivity range, and then the sample is moved and the signal coming from the probe is recorded for each new position. In the latter, the vertical position of the probe is adjusted for each new point of the sample to be analyzed in order to get a signal from the probe equal to a setpoint value, and the height command sent to the probe is the recorded signal. This second operation mode, although more difficult to implement and thus slower, provides two advantages. First, the linearity of the recorded signal is no longer dependent on the physical property being measured (which the experimenter usually cannot control) but on the actuator controlling the height of the probe. Second, the vertical range in which the profiler can be used is greatly increased since it is no longer limited by the bijectivity region of the signal-distance relationship, which is itself dependent upon the physical property being monitored. Instead of requiring that the probe-sample distance stays within the bijectivity range over the *whole* area under investigation, this condition only has to be verified for every two *successive* points.

In this example, we observe that by moving a front-coated mirror in front of the laser focusing lens that the signal read by the photodetector only varies with distance over a range of a fraction of a millimeter, which requires a very precise adjustment of the parallelism between the average plane of the surface to be scanned and the plane in which the sample is translated. In a closed loop configuration, the actuation range of the lens and the application range of the profiler is greatly increased to a few millimeters thanks to the electromagnet.

Going from a sensor indicating with good accuracy the distance from the surface of the sample to a functional scanning-probe microscope requires some digital electronics and software development, as shown in Fig. 6(c). The signal coming from the multi-quadrant photodetector is converted

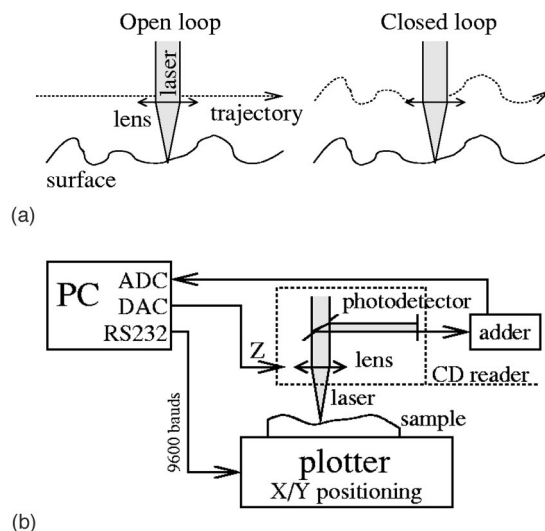


Fig. 6. Two modes for operating a scanning probe microscope: (a) in the open loop configuration, only the value coming from the detector being recorded, and (b) the closed loop configuration, the value read from the sensor being kept constant to a setpoint value by varying the probe-surface distance). (c) Experimental setup: an IBM compatible personal computer fitted with an analog-to-digital converter (ADC) and digital-to-analog converter (DAC) monitors the output of the CD-head photodiodes and controls the lateral position of the sample under the focusing lens in a raster scan motion.

to a digital signal using a 12-bit resolution AD574 analog-to-digital converter (ADC) installed on an ISA card. The command controlling the position of the electromagnet is sent to a 16-bit resolution AD669 digital-to-analog converter (DAC) on an ISA card. The software, written in TURBO PASCAL under DOS, is used to read and store the topography data as well as to synchronize the data acquisition with the translation of the sample as described in Fig. 7.

An alternative to the development of data acquisition and control cards to be connected to the ISA bus of a PC is the use of a microcontroller. A wide range of such chips is now available which only require a limited number of peripheral components to run, after providing analog-to-digital conversion while the digital-to-analog can be built cost-effectively with a network of resistors. The Motorola 68HC11F1 or Hitachi H8/3048F microcontrollers do not require any specific programmer as they can be programmed directly from a standard RS232 port from a PC and are equipped with the required converters for this experiment as well as with a serial port to send commands to the plotter. The development of test circuits for these microcontrollers is beyond the scope of this note: the reader interested in such topics is referred to the documents available at Ref. 14 for further information.

A. Open loop measurements

In order to be able to make open loop measurements, the surface to be scanned must first be positioned under the lens of the CD reader head. Its height is then adjusted while the analog-to-digital converter displays the values read on the output of the photodetector; when a variation of the values becomes visible while the lens-surface distance varies, a usable working setpoint has been reached. Best results are obtained when the setpoint is located on the steepest slope of the signal-distance relationship, located in the middle of the bijective region of this function. The position of the lens is then set, as well as the height of the sample, and the analysis

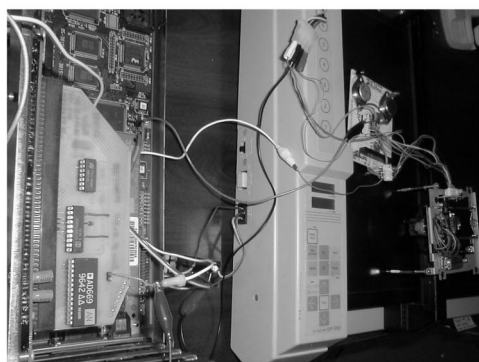
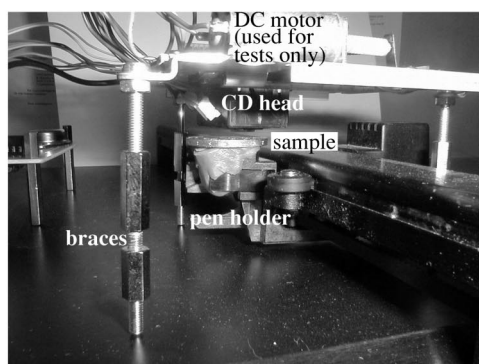
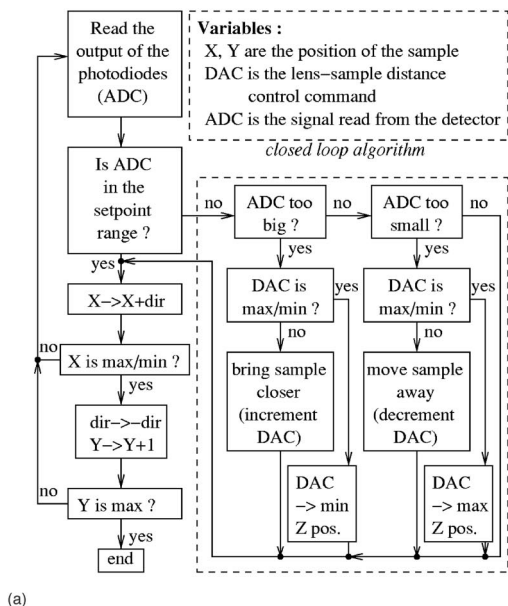
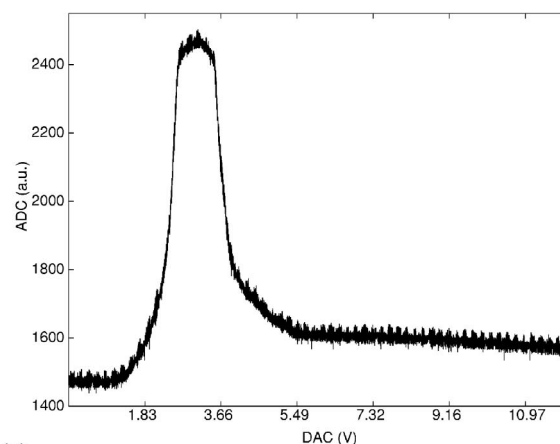
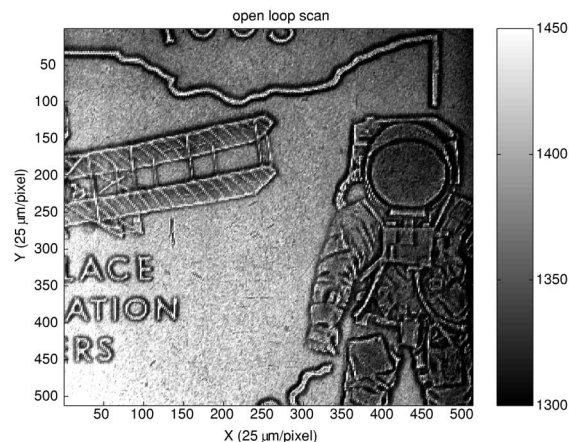


Fig. 7. (a) Algorithm for controlling the instrument. ADC depicts the reading of the analog-to-digital converter, proportional to the sum of the currents going through the photodiodes. When using the open loop operation mode, the value coming from the sensor is recorded, while in the closed loop operation mode we record the current running through the coil of the electromagnet as controlled by the DAC with the ADC being equal to the set-point value. Photographs of the experimental setup: (b) a closeup side-view of the plotter pen-holder to which the coin is fixed using modeling clay as seen on the center of the picture, while the sensor is held over the sample by braces resting on the surface of the plotter for easy adjustment of the height of the CD head and its parallelism with the average plane of the sample. (c) The personal computer controlling the experiment is visible on the left of this top-view photograph, including the AD669-based digital-to-analog conversion ISA card, while the plotter and the electronic circuits related to the laser diode, including the two large 2N3055 power transistors, are visible to the right. The sensor resting over the sample is visible on the far right of this photograph.



(a)



(b)

Fig. 8. (a) Signal-distance relationship and (b) topography of a 25 cent American coin obtained using the open loop algorithm. The peak in the signal-distance curve (a) indicates the position of the coil, as controlled by the DAC, for which the laser is focused on the surface and therefore for which the signal detected by the photodiodes is greatest. The region where the slope of this peak is greatest, for a DAC voltage ranging from 3.5 to 5.5 V here, will lead to the sharpest contrast in the topography image during the scan.

of the sample simply involves translating the surface laterally and monitoring the output of the photodetector for each new position.

Once the scan is completed, we obtain a file including an $N \times N$ matrix which is displayed as a topographic image using the MATLAB function `imagesc` as displayed in Fig. 8.

This imaging mode illustrated in Fig. 6(a) is fast but limited by the sensitivity range of the sensor: if the surface to be analyzed is rougher than this sensitivity range, i.e., the surface comes too close or too far from the lens, the resulting image is saturated, and data on the surface are missing. This problem is worse in the case of an AFM since a surface getting too close to the tip might damage the probe or destroy it by applying too high a force. Furthermore, the force applied to the tip by the sample is not controlled and thus is not constant, leading to nonlinearities in the force-distance relationship, e.g., the forces become attractive or repulsive depending on the distance. As can be seen in Fig. 8(a), the signal-distance relationship is not linear and a calibration relating the measured signal to a physical height is not possible.

B. Closed loop measurements

In this mode, illustrated in Fig. 6(b), instead of keeping the height of the lens constant, the coil electromagnet affixed to the lens is connected to a digital-to-analog converter in order to be able to track the profile of the surface by keeping the signal from the photodiodes constant. Since the output impedance of the DAC or of an operational amplifier used in a follower configuration is too high, a 2N3055 power transistor mounted in current amplifier configuration is added to drive the electromagnet.

This mode is slightly slower than the previous one since it requires an adjustment of the height of the coil for each new point on the surface, but the resulting image is no longer dependent on the signal–distance relationship but only on the actuator–distance relationship, which is much easier to control. Furthermore, the range over which data can be collected is only limited by the means for actuating the lens, which provides an amplitude of a few millimeters in the case of the electromagnet used in the head of a CD reader. The result of such a closed loop scan is presented in Fig. 9.

Of particular interest to us here, the open loop images are of better quality than the images obtained in the closed loop configuration. We attribute this result to the fact that the actuator (the electromagnet controlling the position of the lens) is not appropriate for our application and does not improve the dynamics of the signal, i.e., its operating range, or the linearity of the distance–signal relationship. Furthermore, the limited bandwidth of the reader head implies that a longer delay is needed than the one we used for the position of the lens to stabilize above the sample during the feedback loop. The version of the data acquisition software used here doesn't include any delay between the actuation of the electromagnet and reading the value at the output of the photodiodes, since the acquisition of a whole image is already a very slow process. We still gain in resolution when switching from the open to the closed loop algorithm since the data saved for displaying the topography improve from a 12-bit ADC resolution to a 16-bit DAC resolution. As opposed to the open loop configuration where the relationship between the recorded signal and the topography is dependent on the linearity of the transducer, we can now assume for the closed loop configuration that the displacement of the electromagnet is proportional to the DAC output and provide a proportionality factor between the recorded signal and the topography. The calibration was done using a Veeco Dektak 3030: the height difference between the background plane and the helmet of the astronaut shown in Fig. 9(b) ranges from $87 \pm 15 \mu\text{m}$ (part of the helmet closest to the center of the coin) to $107 \pm 10 \mu\text{m}$ (part of the helmet closest to the border of the coin), leading to a signal to height proportionality factor of $27.5 \pm 0.3 \text{ DAC units}/\mu\text{m}$ or $10.2 \text{ mV}/\mu\text{m}$ for a 16-bit DAC with a $\pm 12\text{-V}$ output range.

We will not describe here the various image-processing steps that are often used to improve the quality of the topographic image acquired. Let us just warn the reader of the risks of generating artifacts when using advanced processing methods. All the images presented in this document are raw data and no data processing has been used for improving the images.

V. CONCLUSION AND PERSPECTIVES

We have used the optical head of a CD reader for building an optical profiler. We have thus been able to experiment

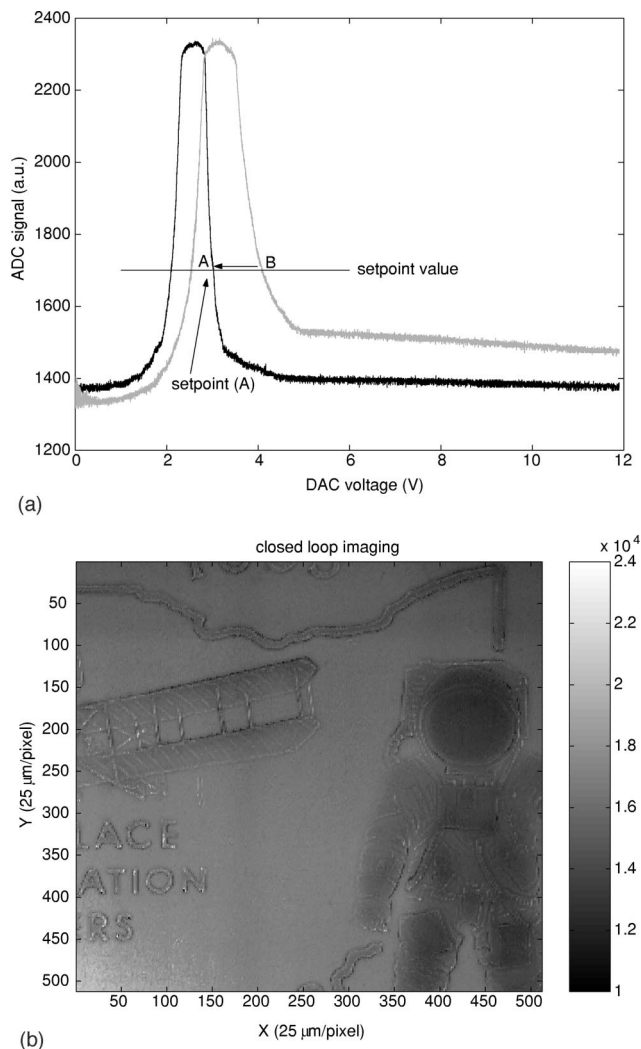


Fig. 9. (a) Signal–distance relationships for two different positions of the lens over the surface and (b) topography of a 25 cent American coin obtained using the closed loop algorithm. While in Fig. 8(a) the signal–distance relationship only provides a calibration information, we here observe how the signal–distance relationship varies over different points of the surface and how the closed loop algorithm, by varying the lens–surface distance, aims at keeping the ADC voltage fixed at the setpoint value represented by point A. The objective of the closed loop algorithm is to move the lens so that point B comes to the position of point A and hence that the gray signal–distance curve overlaps the black one. The control signal applied to the DAC to reach this condition is recorded and plotted on image (b) for all scan positions.

with the actual steps to be followed during the realization of any scanning probe microscope. We have described the various steps for assembling the probe as well as the positioning of the sample relative to the probe, and finally seen what the different operating modes of this instrument are.

In the same way that the first AFM was an extension of the scanning tunneling microscope, it would be possible to improve the lateral resolution of the apparatus described here by including an intermediate probe between the surface and the laser spot. In this case, the laser spot would be used to detect the deflection of a cantilever similar to the one used in an AFM, the latter being directly sensitive to the forces applied by the surface to the tip. This kind of improvement by adding an intermediate probe opens a wide range of possible

extensions of the instrument by choosing an appropriate probe for detecting a physical property other than the topography of the sample.

ACKNOWLEDGMENTS

I thank C. Ferrandez (LPMO/CNRS, Besançon, France) for initial discussions on this project, and L. Francis (IMEC, Leuven, Belgium) for the calibration measurements.

^{a)}Electronic mail: friedtj@free.fr

¹R.A. Young, "Quantitative experiments in electric and fluid flow field mapping," *Am. J. Phys.* **69** (12), 1223–1230 (2001).

²R.J. Behm, N. Garcia, H. Rohrer, and T.G. Vold, "Scanning Tunneling Microscopy and Related Methods," *Am. J. Phys.* **59** (8), 765 (1991).

³R.A. Lewis, S.A. Gower, P. Groombridge, D.T.W. Cox, and L.G. Adorni-Braccesi, "Student scanning tunneling microscope," *Am. J. Phys.* **59** (1), 38–42 (1991).

⁴C. Julian Chen and W.F. Smith, "Introduction to Scanning Tunneling Microscopy," *Am. J. Phys.* **62** (6), 573–574 (1994).

⁵P.J. Williams, D. White, K. Mossman, S. Walker, and G.P. Cant, "A simple scanning tunneling microscope," *Am. J. Phys.* **65** (2), 160–161 (1997).

⁶G. Binnig, H. Rohrer, Ch. Gerber, and W. Weibel, "Surface Studies by

Scanning Tunneling Microscopy," *Phys. Rev. Lett.* **49** (1), 57–61 (1982).

⁷G. Binnig, C.F. Quate, and Ch. Gerber, "Atomic Force Microscope," *Phys. Rev. Lett.* **56** (9), 930–933 (1986).

⁸Y. Martin and H.K. Wickramasinghe, "Magnetic imaging by 'force microscopy' with 1000 Å resolution," *Appl. Phys. Lett.* **50** (20), 1455–1457 (1987).

⁹A.J. Bard, F.R.F. Fan, J. Kwak, and O. Lev, "Scanning Electrochemical Microscope. Introduction and Principles," *Anal. Chem.* **61**, 132–138 (1989).

¹⁰J.P. McKelvey, "Kinematics of the Compact Disc/Digital Audio System," *Am. J. Phys.* **53** (12), 1160–1165 (1985).

¹¹K.C. Pohlman and T.D. Rossing, "The Compact Disc," *Am. J. Phys.* **58** (1), 94 (1990).

¹²F. Perraut Francois, A. Lagrange, P. Pouteau, O. Peyssonneaux, P. Puget, G. McGall, L. Menou, R. Gonzalez, P. Labeye, and F. Ginot, "A new generation of scanners for DNA chips," *Biosens. Bioelectron.* **17** (9), 803–813 (2002); http://www-leti.cea.fr/Commun/Revue_Annuelle/biology&health/FGINOT.PDF

¹³<http://astronomy.swin.edu.au/~pbourke/geomformats/hppl/>: a brief presentation of the HPGL language, including the main commands and their syntax.

¹⁴<http://friedtj.free.fr>: includes tutorials for low cost microcontroller development projects based on the Linux operating system and OpenSource development tools.